Graphical Abstract

Quantifying operating stability in proton exchange membrane fuel cells from voltage measurements: a Lyapunov-inspired approach

Bowen Liang, Huanxia Wei, Mengzhu Shen, Jida Men, Yuan Gao, Tong Zhang, Chaogang Chen, Heping Liang

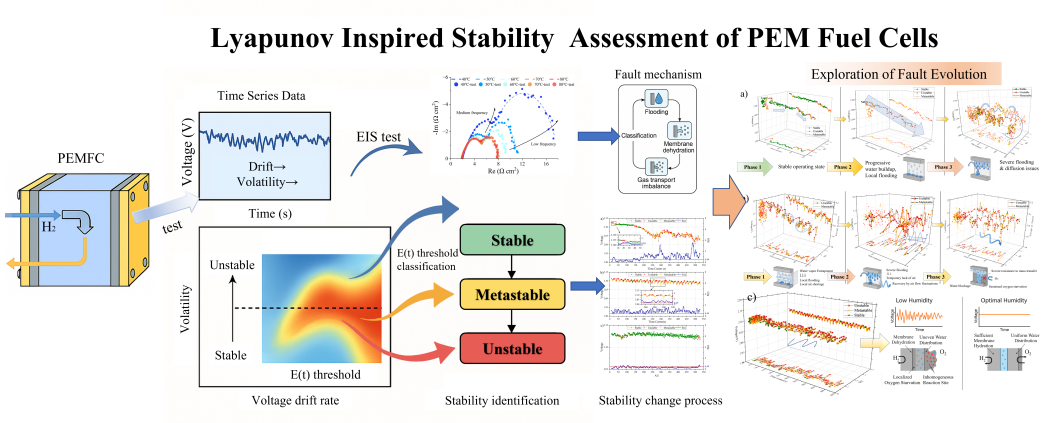

Quantifying operating stability in proton exchange membrane fuel cells from voltage measurements: a Lyapunov-inspired approach

Bowen Liang[a,b,1], Huanxia Wei[a,b,1], Mengzhu Shen[c], Jida Men[a,b], Yuan Gao[a,b,*], Tong Zhang[a,b,d], Chaogang Chen[a,b], Heping Liang[e]

[a] *The New Energy Vehicle Engineering Center, Tongji University, Shanghai, 201804, China*
[b] *School of Automobile Studies, Tongji University, Shanghai, 201804, China*
[c] *Dyson School of Design Engineering, Imperial College London, London, SW7 2AZ, UK*
[d] *Yangtze Delta Region Institute, Tsinghua University, Jiaxing, 314006, Zhejiang, China*
[e] *Y&C Engine Co., Ltd., Jiaxing, 314006, Zhejiang, China*

Abstract

Under constant operating conditions, proton exchange membrane fuel cells (PEMFCs) can exhibit distinct voltage evolution pathways, transitioning between relatively stable, metastable, and unstable regimes depending on the severity of operating conditions. Quantitatively characterizing such non-steady-state voltage behavior remains challenging from a measurement perspective. This study proposes a Lyapunov-inspired measurement methodology for assessing voltage stability in PEMFCs based on time-domain voltage signals. An empirical Lyapunov-like Stability Indicator (LSI) is constructed by combining voltage drift and volatility within a sliding time window, providing a statistically derived indicator of deviations from dynamic equilibrium. The stability boundary is determined using kernel density estimation in the drift-volatility space, enabling data-driven classification of voltage trajectories into stable, metastable, and unstable regimes. The proposed indicator is evaluated using experimental data obtained under 16 systematically varied operating conditions. The results reveal condition-dependent stability patterns: excessive backpressure leads to persistent instability with LSI values

*Corresponding author.
Email address: yuan.gao@tongji.edu.cn (Yuan Gao)
[1] The two authors contribute equally to this work.

frequently exceeding the identified threshold, whereas optimal humidification conditions maintain the voltage predominantly within the stable regime. By linking the classified voltage regimes with electrochemical impedance spectroscopy measurements, the analysis provides additional insight into possible stage-wise fault evolution processes, including flooding, membrane dehydration, and gas transport imbalance. The proposed framework provides a physically interpretable measurement indicator for characterizing voltage stability in PEMFCs and supporting stability-oriented monitoring and diagnostic analysis in electrochemical energy systems.

Keywords: Proton exchange membrane fuel cell, Lyapunov-inspired indicator, Voltage stability, Electrochemical impedance spectroscopy, Measurement methodology

---

Nomenclature

AC Alternating Current

DRT Distribution of Relaxation Times

EIS Electrochemical Impedance Spectroscopy

GDL Gas Diffusion Layer

ICE Individual Conditional Expectation

K-K Kramers-Kronig

LSTM Long Short-Term Memory

MSE Mean Squared Error

ORR Oxygen Reduction Reaction

PEM Proton Exchange Membrane

PEMFC Proton Exchange Membrane Fuel Cell

MEA Membrane Electrode Assembly

R^2 Coefficient of Determination

CNN Convolutional Neural Network

BPNN Back Propagation Neural Network

RF Random Forest

RL Reinforcement Learning

SVM Support Vector Machine

LSI Lyapunov-like Stability Indicator

KDE Kernel Density Estimation

T Temperature (°C)

RH Relative humidity

λ_{ca} Cathode stoichiometry

λ_{an} Anode stoichiometry

S_1 First-order Sobol index

S_T Total Sobol index

R_0 Ohmic resistance (Ω cm^2)

R_{pol} Polarization resistance (Ω cm^2)

$g(\tau)$ Time relaxation distribution (Ω cm^2)

τ Time constant (s)

$\gamma(\ln \tau)$ Time relaxation distribution (Ω cm^2)

Z_{Re} Real part of impedance (Ω cm^2)

Z_{Im} Imaginary part of impedance (Ω cm^2)

Z'_{Re} Real part of fitted impedance (Ω cm^2)

Z'_{Im} Imaginary part of fitted impedance (Ω cm^2)

$|Z(\omega)|$ Magnitude of impedance (Ω cm^2)

$\Delta Re(\omega)$ Residual of real part (%)

$\Delta Im(\omega)$ Residual of imaginary part (%)

D^b Bootstrapped dataset

B Total number of trees

h_b Prediction from the b-th tree

$\mathrm{Var}(Y)$ Total variance

1. Introduction

Proton Exchange Membrane Fuel Cells (PEMFCs) have emerged as a promising clean energy technology owing to their high energy conversion efficiency and zero harmful emissions [1]. By converting chemical energy directly into electricity, with water as the only by-product, PEMFCs offer a promising solution toward decarbonized energy systems [2]. However, under constant external conditions, PEMFCs occasionally exhibit voltage decay and complex fluctuations. These behaviors reflect complex multi-physics interactions, encompassing electrochemical kinetics [3], gas transport [4] , and water management [5].

Previous studies have demonstrated that voltage time series encode rich information relevant to cell health and failure evolution. Voltage deviations, whether slow recession or high-frequency noise, often signal underlying issues such as flooding [6], membrane drying [7, 8], or catalyst degradation [9]. For instance, Yang et al. [10] applied voltage undershoot and voltage recession as evaluation indices to assess the voltage stability. Tang et al. [11] developed a probabilistic approach to quantify voltage fluctuations for fault detection. Li et al. [12] proposed airflow interruption tests to identify hydrogen leakage by analyzing voltage drop duration. Zhao et al. [13] used an entropy-based method to extract voltage fluctuations for fuel cell health evaluation, establishing a three-level health management strategy based on thresholds. More recently, data-driven methods have gained traction. Benouioua et al. [14] employed instantaneous frequency and voltage envelope features for fault classification using machine learning models. Li et al. [15] used a least squares support vector machine to extract spatiotemporal features, including voltage, for high-precision multi-fault diagnosis. Liu et al. [16] converted one-dimensional voltage sequences into two-dimensional images using signal-to-image transformation and applied K-means clustering to distinguish between flooding and dehydration conditions. While effective, these methods often operate as black boxes, lacking physical interpretability and remaining constrained by binary fault and non-fault paradigms.

Moreover, these methods typically focus on fault identification after degradation has occurred, often overlooking the continuous, multi-stage evolution of system dynamics leading up to failure. Voltage instability in PEMFCs is not an abrupt event, but rather a progressive deviation from equilibrium [17]. When a step change occurs in current density, the redistribution of overpotentials at the anode and cathode breaks the dynamic equilibrium

at the electrode-electrolyte interface, triggering transient voltage responses. Under ideal conditions of well-controlled temperature, humidity, and backpressure, voltage evolution is expected to be smooth and stable. However, deviations from these conditions can lead to drift and volatility in the voltage signal, indicating dynamic instability [18]. The temporal characteristics of voltage signals vary considerably under different operational conditions, such as temperature, humidity, and backpressure. Xiao et al. [7] employed Electrochemical Impedance Spectroscopy (EIS) to analyze the effects of cathode backpressure, stoichiometric ratio, and cell temperature on membrane dehydration. Their results reveal impedance variations and the temporal evolution of membrane drying under different operating conditions. Ren et al. [19] investigated the relationship between ohmic resistance and flooding process, identifying characteristic changes in zero-phase resistance during water accumulation. Shao et al. [20] used numerical modeling to reconstruct the internal state evolution of PEMFCs under varying operational conditions and examined the phenomenon of steady-state multiplicity. Hu et al. [21] adopted a system modeling approach to analyze the dynamic responses of cell voltage and membrane water content, finding that high ambient pressure increases both the decay rate and the recovery rate of cell voltage. Recently, Sun et al. [22] employed a hybrid ensemble learning model to analyze how temperature, pressure, and humidity affect PEMFC external characteristics, showing that elevated temperature can improve voltage output whereas medium humidity is more favorable for stable performance. Sun et al. [23] further developed a boosted deep neural network model for forecasting electrochemical impedance under varying operating conditions and reported that elevated temperature and pressure can reduce impedance by improving proton conductivity and reaction kinetics at low current densities.

Despite extensive research on diagnostics and degradation analysis of PEMFCs, the concept of operational stability has received comparatively limited systematic investigation. Most existing studies focus on fault detection or performance degradation after observable symptoms emerge, typically relying on predefined thresholds or empirical signatures such as voltage drops, noise patterns, or efficiency losses. While these approaches are effective for identifying faults once they occur, they provide limited insight into how fuel cell performance gradually evolves under sustained but suboptimal operating conditions, such as low humidity or excessive backpressure. In practice, fuel cell failure is rarely an instantaneous event. Instead, it often results from a progressive deviation from dynamic equilibrium caused by changes in coupled

electrochemical, thermal, and mass transport processes. Capturing this gradual transition remains challenging, as conventional diagnostic indicators are generally designed for discrete fault detection rather than continuous characterization of dynamic system behavior. From a measurement perspective, this highlights the need for quantitative indicators capable of describing how voltage signals evolve over time and how these changes relate to the underlying stability of fuel cell operation. It is important to distinguish stability assessment from traditional fault diagnosis. While fault diagnosis aims to identify and classify degraded or failed states, stability analysis focuses on the system's ability to maintain consistent operation in the presence of internal fluctuations and external perturbations. A stability-oriented perspective therefore provides complementary information to conventional diagnostics by emphasizing the evolution of system behavior before clear fault signatures appear. Such information can be valuable for engineering applications, where early indicators of instability may support improved operational monitoring, predictive maintenance, and risk mitigation.

Motivated by this need, this study proposes a Lyapunov-inspired measurement indicator for assessing voltage stability in PEMFCs using voltage time-series data. An empirical Lyapunov-like Stability Indicator (LSI) is constructed by combining two statistical characteristics of voltage dynamics—long-term drift and short-term volatility—within a sliding time window. The indicator provides a quantitative description of deviations from dynamic equilibrium and enables continuous tracking of voltage stability under constant operating conditions. Based on the statistical distribution of these two quantities in the drift–volatility space, a stability boundary is determined using kernel density estimation, allowing voltage trajectories to be categorized into three regimes: stable, metastable, and unstable. This regime-based representation provides a practical framework for describing intermediate states between stable operation and severe degradation, which are often difficult to capture using binary fault classifications. To further explore the physical implications of these regimes, the voltage-based stability analysis is combined with EIS measurements obtained under a range of operating conditions. The joint analysis of time-domain voltage behavior and frequency-domain electrochemical response provides additional insight into how different operating conditions influence fuel cell dynamics and potential degradation pathways.

Overall, the proposed approach provides a measurement-based framework for quantifying voltage stability in PEMFCs using voltage time-series data. By integrating the Lyapunov-inspired stability indicator with EIS, the study

establishes a joint time–frequency analysis perspective for examining voltage dynamics and their associated electrochemical responses. This combined analysis supports the monitoring of stability behavior under diverse operating conditions and contributes to the development of stability-oriented diagnostic and monitoring strategies for fuel cell systems.

2. Experimental study

2.1. Experimental setup

This study investigates a custom-assembled proton exchange membrane fuel cell stack composed of three fuel cells, each with an active area of 300 cm^2, with a total rated power close to 1 kW. The stack employs commercial Membrane Electrode Assemblies (MEAs), featuring a 12 μm-thick proton exchange membrane and a platinum catalyst loading of 0.35 mg/cm^2 on both electrodes. Metal bipolar plates are applied, incorporating a single-serpentine flow field on the anode side and straight flow channels on the cathode side. The stack endplates are equipped with six 3/8-inch ports, which serve as inlets and outlets for anode gas, cathode gas, and coolant flow. Having undergone intermittent operation for approximately one year, the stack exhibits clear signs of performance degradation, providing favorable conditions for observing voltage instability and fault-prone behavior under various operating scenarios.

The test platform integrates a 2 kW electronic load with a voltage range of 0.1-40 V and a current range of 0-600 A, offering a voltage resolution of 1 mV, a current resolution of 10 mA, and a current response time of less than 50 μs. Gas humidification is achieved through a combination of bubbling and spray techniques, with the dew-point temperature controlled within ± 1 °C, resulting in a relative humidity measurement uncertainty of less than 1%. Backpressure regulation is implemented via a diaphragm-type valve located at the cathode outlet, operating in a pulse-discharging control mode that maintains pressure accuracy within ± 2 kPa. Stack temperature is managed by a dual-loop water-cooling system, where deionized water circulates internally while an external loop dissipates heat, maintaining temperature stability within ± 1 °C. Electrochemical impedance spectroscopy (EIS) is performed using a KIKUSUI impedance analyzer, covering a frequency range from 10 mHz to 20 kHz. An AC perturbation amplitude equal to 8% of the corresponding DC operation current is applied. Ten data points are acquired per frequency decade, and each point is averaged over eight repeated

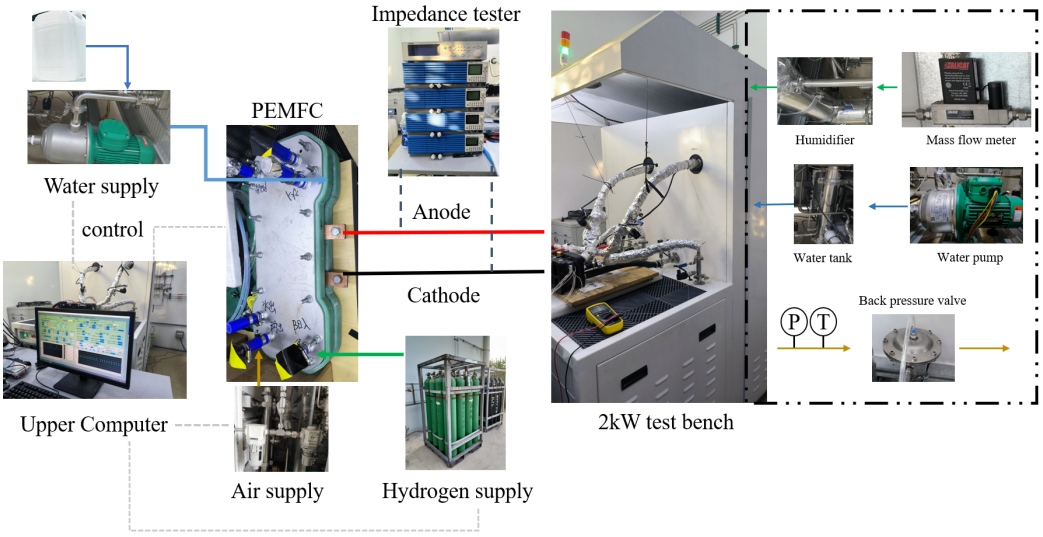

Figure 1: PEMFC and testing bench.

measurements to reduce stochastic noise and improve data reliability. These measurement resolutions and control accuracies provide the experimental basis for consistently extracting the drift and volatility statistics used in the LSI framework. The experimental setup is shown in Figure 1.

Figure 1 illustrates the experimental test bench designed for a 2 kW fuel cell stack, featuring an electronic load range of 0 to 600 A and a voltage range of 0.1 to 40 V. The stack is water-cooled to regulate its thermal conditions. The platform utilizes a dual-loop cooling system: an internal deionized water circuit, which humidifies the gas and cools the stack, and an external cooling water loop, which removes heat via a heat exchanger interfacing with the internal circuit. Gas humidification is achieved through a combination of bubbling and spraying techniques, while heating tapes are used to regulate the intake air temperature. The humidity of the supplied gases is controlled by adjusting the dew-point temperature and preheating of the inlet air. The flow rates of hydrogen and air are precisely controlled using mass flow controllers. A diaphragm-type backpressure valve located at the stack outlet maintains the desired gas pressure within the circuit. Additionally, a gas-liquid separator is installed on the anode side to minimize the impact of anode flooding, thereby enhancing stack performance and maintaining voltage stability. To further investigate the internal electrochemical processes, EIS is conducted using a KIKUSUI impedance analyzer (10 mHz to 20 kHz

frequency range).

2.2. Experimental procedure

To systematically investigate the effects of external operating conditions on PEMFC voltage stability, this study adopts a controlled single-variable experimental design. The three key factors (temperature, relative humidity, and backpressure) are individually varied, while the other two are held constant at conditions known to support stable and optimal operation. Specifically, temperature and humidity are fixed at 70 °C and 90 % Relative Humidity (RH), respectively, while backpressure is maintained at atmospheric pressure when not under investigation. This protocol ensures that the influence of each variable on voltage stability can be independently evaluated, minimizing cross-interference. Prior to each test, the PEMFC stack operates under open-circuit conditions to allow stabilization of temperature, humidity, and pressure control subsystems. Once the predefined setpoints are reached and confirmed stable, the stack is transitioned to galvanostatic operation at a current density of 100 mA/cm^2 for 180 s, ensuring thermal and electrochemical equilibrium. Following this pre-conditioning period, the current is increased to 200 mA/cm^2 to initiate the primary observation phase. During this phase, voltage signals are continuously recorded over a 540 s interval to capture both transient and steady-state characteristics under the given operation condition. This observation window was selected to capture the onset of instability and its subsequent evolution under the chosen operating conditions while keeping the external boundary conditions effectively constant during each test. Approximately 60 seconds into this phase, EIS is performed in situ using a KIKUSUI impedance analyzer, covering a frequency range from 10 mHz to 20 kHz, with an AC perturbation amplitude of 8 % of the DC current. After each test cycle, the fuel cell is safely shut down and purged, and external parameters are reconfigured for the next test case. This standardized procedure enhances repeatability and consistency across all tests, forming a robust dataset for assessing voltage behavior using the proposed LSI. The complete set of tested operating conditions is summarized in Table 1. Several conditions are intentionally extended into non-ideal or extreme regimes, allowing the capture of fault-prone and instability-prone behaviors. The selected ranges of temperature (40–80 °C), relative humidity (40–100%), and backpressure (0–125 kPa) cover the typical operating conditions reported for PEMFC systems in experimental studies. The experiments are primarily conducted in the low-to-medium current density region, where

voltage stability variations can be clearly observed while avoiding severe stack protection or safety risks associated with very high loads.

Table 1: Different operating conditions

Parameters	**Operating levels**	**Constant parameters**
Current (mA/cm^2)	200	–
Stack temperature (°C)	40, 50, 60, 70, 80	RH = 90 %, P = 0 kPa
Humidity (%)	40, 50, 60, 70, 80, 90, 100	T = 70 °C, P = 0 kPa
Backpressure (kPa)	50, 75, 100, 125	T = 70 °C, RH = 90 %

2.3. LSI for PEMFC voltage dynamics

In classical control theory, Lyapunov stability provides a foundational approach for assessing the dynamic behavior of nonlinear systems. A system is considered Lyapunov stable if small perturbations from equilibrium lead to bounded responses over time, and asymptotically stable if such deviations eventually vanish and the system returns to its equilibrium state. Mathematically, Lyapunov's direct method is based on the existence of a scalar Lyapunov function V(x) that is positive definite and whose time derivative along system trajectories is negative semi-definite, i.e., $\dot{\mathrm{V}}\left(x\right) \leq 0$. However, in complex electrochemical energy systems such as PEMFCs, deriving a first-principles dynamic model that explicitly satisfies Lyapunov conditions is often intractable. This difficulty arises from the nonlinear, multiscale couplings among mass transport, electrochemical kinetics, water management, thermal effects, and other internal processes. In particular, the output voltage evolution under different operating conditions often reflects latent phenomena such as localized flooding, membrane dehydration, and reactant starvation, whose governing dynamics are not fully captured by existing models.

To address this challenge, this study introduces a data-driven empirical framework inspired by Lyapunov stability theory. Instead of analytically deriving a Lyapunov function from explicit state equations, a Lyapunov-like Stability Indicator (LSI), whose time-dependent value is expressed as $E(t)$, is inferred directly from measurable voltage time series using a sliding window strategy. This indicator function characterizes the local behavior of the signal by integrating short-term voltage drift and high-frequency volatility within

a localized time window:

$$E(t) = \alpha \cdot |\mu'(t)| + \beta \cdot \sigma(t), \tag{1}$$

where $\mu'(t)$ denotes the local temporal slope of voltage within the window, $\sigma(t)$ is the corresponding standard deviation, and α, β are empirical scaling factors used to balance sensitivity. This formulation is motivated by both practical observations and physical expectations: under well-regulated, quasi-steady-state operating conditions, a PEMFC is expected to exhibit voltage signals with negligible trend and low temporal variability. In contrast, deviations from this nominal behavior, arising from gradual degradation, reactant imbalance, membrane drying, or localized flooding, typically manifest as either slow but persistent voltage drift or high-frequency noise and oscillation. The drift term effectively captures long-term directional trends potentially associated with irreversible processes, while the volatility term reflects short-term, high-frequency variations commonly linked to transient local disturbances. The combination of both components into LSI therefore provides a two-timescale characterization of voltage instability. Furthermore, this construction bears conceptual resemblance to classical Lyapunov functions, as it implicitly penalizes deviations from ideally flat and noise-free voltage trajectories. An increasing LSI value indicates divergence from equilibrium, whereas a decreasing LSI value suggests convergence or recovery toward a stable operating state.

Therefore, this formulation constitutes a data-driven Lyapunov-like framework, in which the temporal smoothness and regularity of observable output trajectories serve as proxies for latent system stability. This conceptual alignment bridges physical interpretability with data-driven diagnostics, enabling robust, real-time assessments even when internal state variables or governing equations are unavailable or only partially known. Moreover, by calculating the temporal derivative of the indicator, denoted $\frac{dE}{dt}$, it becomes possible to further distinguish between different dynamic regimes:

$$\begin{aligned} \text{Stable: } & E(t) < \theta_E, \\ \text{Metastable: } & E(t) \geq \theta_E, \quad \frac{dE}{dt} \leq 0 \\ \text{Unstable: } & E(t) \geq \theta_E, \quad \frac{dE}{dt} > 0 \end{aligned} \tag{2}$$

where θ_E is a statistically derived threshold. In this formulation, the classification of stable, metastable, and unstable regimes is first defined math-

ematically based on the magnitude of the instability indicator E(t) and its temporal evolution. The stable regime corresponds to situations where E(t) remains below the stability threshold, indicating that both voltage drift and voltage fluctuations remain within statistically bounded limits. When E(t)

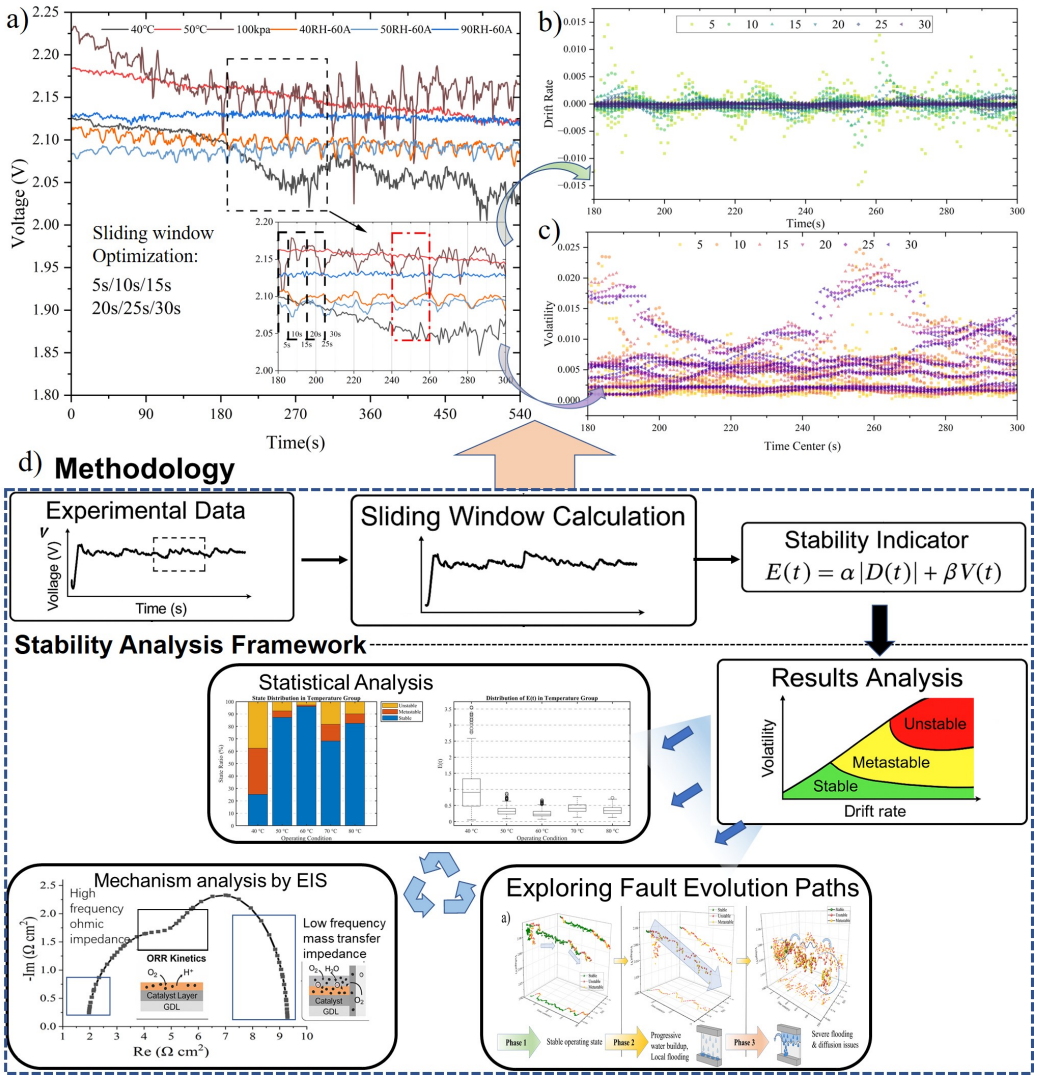

Figure 2: Methodology and stability analysis framework: (a) voltage profiles under typical conditions, (b) drift rate evolution with varying window lengths, (c) voltage volatility with varying window lengths, and (d) integrated workflow for Lyapunov-like stability assessment and fault diagnosis.

exceeds this threshold, the system enters a non-stable region. Within this region, the temporal derivative dE/dt is used to distinguish different dynamic behaviors. The metastable regime corresponds to cases where the instability level does not continue to increase ($dE/dt \leq 0$), suggesting that the abnormal behavior remains bounded or transient. In contrast, the unstable regime corresponds to situations where the instability indicator continues to increase (dE/dt >0), indicating a progressive deterioration of voltage stability. From an engineering perspective, these regimes represent different levels of operational risk. The stable regime corresponds to normal operation without the need for intervention. The metastable regime indicates the emergence of abnormal voltage fluctuations and can be interpreted as a warning stage where the system should be monitored more closely. The unstable regime, in contrast, represents a higher-risk condition characterized by sustained instability, where operational adjustments or protective actions may be required to prevent further degradation.

In practice, the computation of drift rate and voltage volatility depends critically on the sliding window length N, which defines the temporal resolution of $E(t)$. Specifically, at each central time point t_k, the drift rate $\mu'(t_k)$ and volatility $\sigma(t_k)$ are computed as follows:

$$\begin{aligned} \mu'(t_k) &= \frac{\sum_{i=1}^{N}(t_i - \bar{t})\big(\mathrm{V}_i - \bar{\mathrm{V}}\big)}{\sum_{i=1}^{N}(t_i - \bar{t})^2}, \\ \sigma(t_k) &= \sqrt{\frac{1}{N}\sum_{i=1}^{N}\big(\mathrm{V}_i - \bar{\mathrm{V}}\big)^2}, \end{aligned} \tag{3}$$

where $\mathrm{V_i}$ denotes the voltage value at the i-th time step within a sliding window, and t_i represents the corresponding time point of $\mathrm{V_i}$. The symbols $\bar{V}$ and $\bar{t}$ are the mean values of voltage and time within the current window, respectively, and N is the number of samples per window.The choice of window length must be adapted to the temporal dynamics of the fuel cell system, as it directly affects the statistical reliability of both voltage drift and volatility estimation. To evaluate the robustness of this parameter, a sensitivity analysis is conducted using several candidate window lengths. As illustrated in Figure 2, six window sizes (5 s, 10 s, 15 s, 20 s, 25 s, and 30 s) are examined under representative voltage operating conditions. With increasing window size, the computed drift and volatility estimates become progressively smoother but less sensitive to subtle temporal variations in the

voltage signal. Conversely, overly short windows amplify stochastic fluctuations and increase the randomness of the volatility estimates, which compromises the stability of the statistical characterization. The results show that very short windows (5–10 s) lead to unstable statistical estimates, whereas excessively long windows ($\geq$ 30 s) overly smooth the voltage evolution and reduce sensitivity to dynamic changes. Within the intermediate range of 15–25 s, both drift and volatility statistics exhibit relatively stable distributions, indicating that the LSI values remain consistent under moderate variations in window length. Based on this sensitivity analysis, a 20 s window with a 1 s step size is adopted as a representative configuration that provides a balanced compromise between responsiveness to voltage dynamics and robustness of statistical estimation. The complete methodological workflow is depicted in Figure 2d, which outlines the implementation of the proposed Lyapunov-inspired stability assessment. The procedure includes voltage signal preprocessing, dynamic state classification, statistical evaluation of the LSI, and interpretation of the results in relation to operating conditions and electrochemical impedance characteristics. By structuring the analysis around experimentally measured voltage signals, the proposed framework provides a measurement-oriented methodology for characterizing voltage stability in PEMFC systems, enabling systematic interpretation of stability behavior across different operating conditions.

3. Results and discussion

This section integrates the proposed LSI with experimental voltage observations to analyze the dynamic behavior of PEMFCs under various external operating conditions. The classification outcomes across all test scenarios are statistically summarized to quantify voltage stability levels under different control parameters. In addition, EIS is employed to explore the physicochemical mechanisms associated with voltage instability, thereby providing a mechanistic interpretation of the observed dynamic phenomena.

3.1. Calibration and validation of the LSI

The systematic construction of the LSI involves the identification and validation of key design parameters, including the weighting coefficients assigned to the drift rate and volatility, as well as the data-driven determination of the stability threshold θ_E. These elements form the analytical foundation

for translating observed voltage fluctuations into discrete dynamic stability states.

Figure 3a presents a state-space distribution of voltage trajectories under 16 experimental conditions, projected onto the volatility-drift feature space. To eliminate transient effects immediately following step changes in current, such as voltage undershoot and recovery, a 10-second segment after each transition is excluded. This preprocessing ensures that the LSI reflects quasi-steady-state voltage behavior. Under favorable operating conditions, both drift and volatility remain low, with data points tightly clustered near the origin, indicating stable system dynamics. In contrast, under destabilizing scenarios (Condition 9), the trajectories exhibit wide dispersion and elevated values in both drift and volatility, consistent with divergent and unstable dynamic evolution.

Weighting coefficients are introduced to balance the contributions of voltage drift rate and voltage volatility in the stability indicator. Statistical analysis of the measured voltage data shows that the typical magnitude of the drift rate is approximately one order of magnitude smaller than that of the volatility term. Without appropriate scaling, the volatility component would dominate the indicator and weaken the influence of the drift term. Therefore, the coefficients are set to $\alpha = 10$ and $\beta = 1$ to compensate for this magnitude difference and ensure comparable contributions of the two variables. Under this scaling, the indicator captures both the long-term voltage trend reflected by the drift rate and the short-term stochastic fluctuations represented by the volatility. For improved numerical interpretability and visualization, the value of $E(t)$ is uniformly scaled by a factor of 100. This adjustment preserves the underlying physical interpretation while facilitating consistent visual comparison across different experimental conditions.

To determine the stability threshold θ_E, a probabilistic approach based on relative density estimation is applied, instead of relying on absolute values that are sensitive to localized fluctuations and noise. Specifically, a two-dimensional Kernel Density Estimation (KDE) is performed over the state space defined by drift rate and voltage volatility. The resulting probability field is visualized in Figure 3b as a series of concentric probability density contours, corresponding to the 90%, 75%, 50%, 25%, and 10% quantiles. These contours represent progressively lower probability regions, extending outward from the high-density core near the origin. As the relative density decreases, the distribution of state points becomes increasingly scattered, indicating greater variability and deviation from typical operating states.

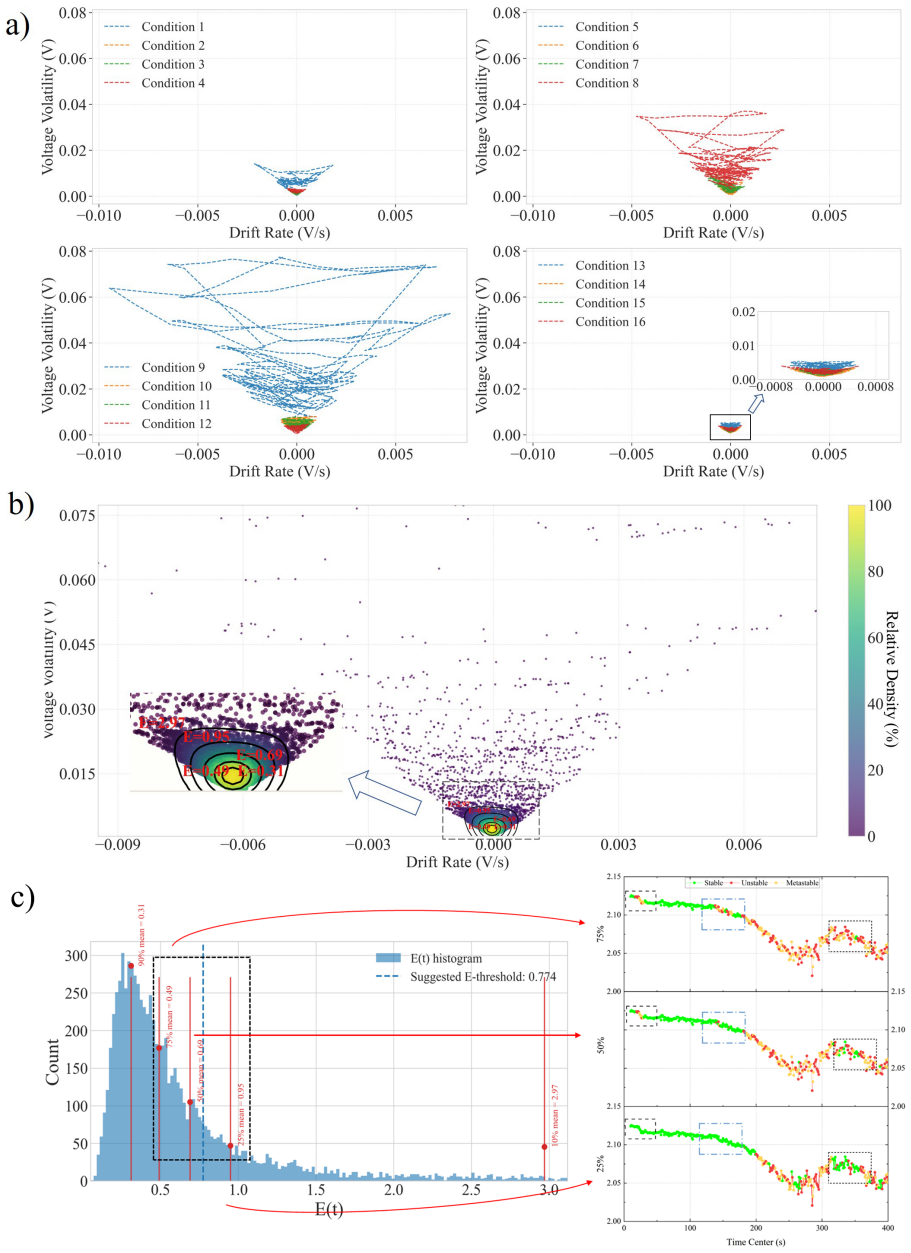

Figure 3: State-space representation of PEMFC voltage behavior: (a) drift-volatility trajectories under various operating conditions, and (b) kernel density distribution of voltage states in drift-volatility space.

From a physical standpoint, a well-regulated fuel cell operating under quasi-steady-state conditions tends to produce voltage trajectories with low drift and low volatility, leading to a dense cluster of state points near the origin. In contrast, when disturbances such as membrane dehydration, flooding, or reactant starvation occur, both drift and volatility increase, and the corresponding points disperse into lower-density regions of the state space. This outward shift reflects a physical transition from stable to metastable or unstable dynamic regimes.

Leveraging this spatial pattern, it is observed that higher-probability KDE contours provide finer resolution for detecting early signs of instability. However, using overly conservative thresholds near the density peak may lead to false positives, by misclassifying normal stable fluctuations as signs of instability, especially under typical operational variability. To further formalize the threshold determination, a KDE-elbow method was applied to the distribution of $E(t)$. Specifically, the elbow point was identified by locating the maximum perpendicular distance from the cumulative mean $E(t)$-percentile curve to its chord, which corresponds to the natural transition between high-density low-energy regions and low-density high-energy regions. This analysis yielded an elbow threshold of ($E = 0.774$). In the histogram of $E(t)$, the closest percentile layers to this value are 75%, 50%, and 25%, which were therefore considered as candidate thresholds. A comparative evaluation was then performed under a typical low-temperature operating condition. As shown in the right panel of Figure 3c, all three thresholds can detect the pronounced voltage drop between 200 s and 300 s. However, as the threshold decreases, the ability to resolve early anomalies also deteriorates. At the 25% density layer, the mild voltage decline around 25 s is not captured, whereas both the 50% and 75% thresholds successfully detect it. Further comparison between the 50% and 75% thresholds reveals that the 75% threshold captures the slow but low-fluctuation decline around 150 s more effectively, while the 50% threshold fails to do so. Moreover, in the high-volatility period after 300 s, the 75% threshold provides a more consistent delineation of risk intervals, whereas the 50% and 25% thresholds tend to misclassify certain stable periods. Considering both statistical justification and empirical performance, the 75% KDE contour is adopted as the decision boundary, as it allows earlier and more comprehensive detection of incipient anomalies. Accordingly, the stability threshold (θ_E) is defined as the mean E(t) of all data points enclosed within this contour. Although this boundary is derived from a data-driven KDE distribution, sensitivity analysis demonstrates that when the contour

level varies within a relatively wide range (25–75%), the major instability intervals identified in the voltage evolution remain largely consistent. This observation indicates that the proposed stability classification exhibits strong robustness against moderate variations in data density and noise.

To further demonstrate the practical relevance of the LSI, it is applied to representative voltage time series under three typical operating conditions: low temperature, low humidity, and nominal operation. The resulting voltage trajectories and corresponding time-dependent value $E(t)$, reflecting the LSI response, are presented in Figure 4, with dynamic states labeled as stable, metastable, or unstable regimes.

Figure 4a illustrates the voltage profile under low-temperature operation, where the system initially maintains a relatively steady state. Around 20 seconds, the voltage begins to decline, setting onto a plateau near 2.11 V. During this transition, the LSI time-dependent value $E(t)$ exhibits minor fluctuations above the stability threshold θ_E, indicating the incipient deviation from equilibrium. As operation continues, instability becomes more pronounced: at approximately 125 s, the voltage starts to decline more sharply, and by 175 s, $E(t)$ clearly exceeds the threshold, marking the onset of a persistently unstable regime. The system then oscillates between metastable and unstable states, reaching a voltage nadir near 270 s, which coincides with a peak in $E(t)$. Although a partial voltage recovery is observed afterward, significant fluctuations persist and $E(t)$ remains elevated, correctly indicating that the system remains non-steady. Beyond 470 s, further performance deterioration is observed. This case demonstrates the ability of the LSI to capture both early-stage degradation and complex recovery-relapse dynamics, without overestimating transient improvements. The strong temporal alignment between peaks in $E(t)$ and voltage downturns under low-temperature operating conditions highlights its effectiveness in detecting critical dynamic deviations from nominal behavior, even without direct assess to internal system states.

Under low-humidity conditions (Figure 4b), the voltage profile exhibits clear periodic oscillations, likely caused by intermittent membrane dehydration and water redistribution. The corresponding LSI value $E(t)$ responds with synchronized, threshold-crossing fluctuations, indicative of alternating stability states. A magnified view between 240-320 s reveals three full oscillation cycles, during which the system transitions repeatedly between metastable and unstable states. The alignment between the voltage waveform and $E(t)$ supports the indicator's effectiveness in capturing recurrent

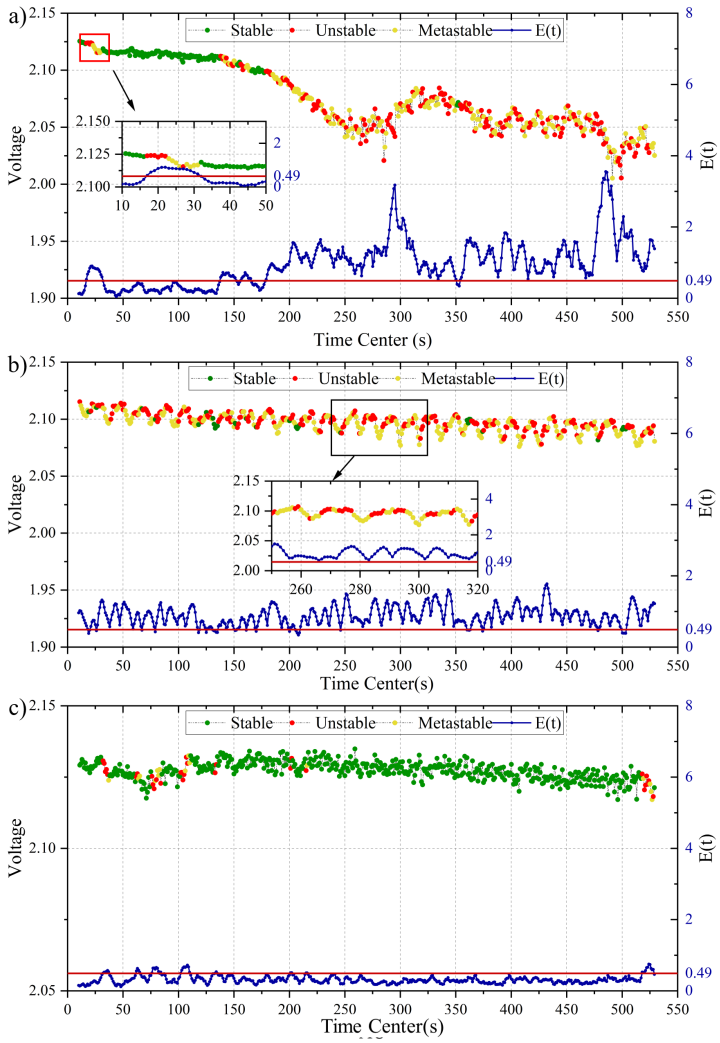

Figure 4: Application of the LSI value $E(t)$ to representative voltage trajectories: (a) divergence under low temperature, (b) cyclic instability under low humidity, (c) nominal stability under normal conditions.

dynamic transitions and temporal complexity in system behavior. Figure 4c displays a case under nominal operating conditions, where the voltage remains generally stable with only small random perturbations. The corresponding $E(t)$ values stay consistently close to the baseline and rarely exceeds the stability threshold θ_E. In this case, the classification is dominated by stable states (green), with only a few isolated points approaching the in-

stability boundary. This scenario confirm the LSI's robustness in the absence of external disturbances and its reliability in steady-state validation.

Taken together, these results show that the proposed LSI serves as a physically interpretable and dynamically sensitive metric for classifying voltage behavior in PEMFC systems. By combining drift rate and volatility, LSI captures both long-term trends and short-term fluctuations, enabling the detection of critical dynamic transitions, such as incipient failure, metastable cycling, and progressive divergence. These capabilities highlight the strong potential of this indicator for real-time health monitoring and early fault diagnostics in PEMFCs.

3.2. Temporal evolution and statistical characterization

This section further examines its behavior of the proposed LSI across a range of representative PEMFC operating conditions. Rather than analyzing isolated scenarios, the focus here is on how the overall stability landscape evolves through the systematic variation of environmental parameters, namely temperature, backpressure, and humidity.

Figure 5 presents a unified comparison of PEMFC voltage behavior and the corresponding responses of LSI value $E(t)$ under systematically varied operating conditions. Each subplot illustrates voltage time series corresponding to a single operating condition (temperature, backpressure, and humidity). Voltage states are color-coded as green (stable), yellow (metastable), and red (unstable), while the associated $E(t)$ values are visualized as vertical bars. A horizontal gray plane denotes the stability threshold θ_E, enabling direct evaluation of both transient deviations and persistent instability across varying test conditions.

In Figure 5a, temperature emerges as a key factor influencing PEMFC voltage dynamics, which is consistent with the non-monotonic temperature dependence reported by Fu et al. [24]. At moderate temperatures (50-70 °C), voltage profiles are generally smooth, with the majority of $E(t)$ values remaining below the stability threshold θ_E, indicating overall stable operation. At 50 °C, the voltage gradually declines from approximately 2.175 V to 2.10 V, likely reflecting a slow transition toward thermal equilibrium. Despite minor transient deviations the system remains within the stable regime. As the temperature increases to 70 °C, the cell voltage reaches its peak, driven by enhanced electrochemical reaction rates. However, this improvement is accompanied by noticeable oscillations, with more frequent excursions of $E(t)$ above the threshold, signaling a reduction in voltage robustness. While 70 °C

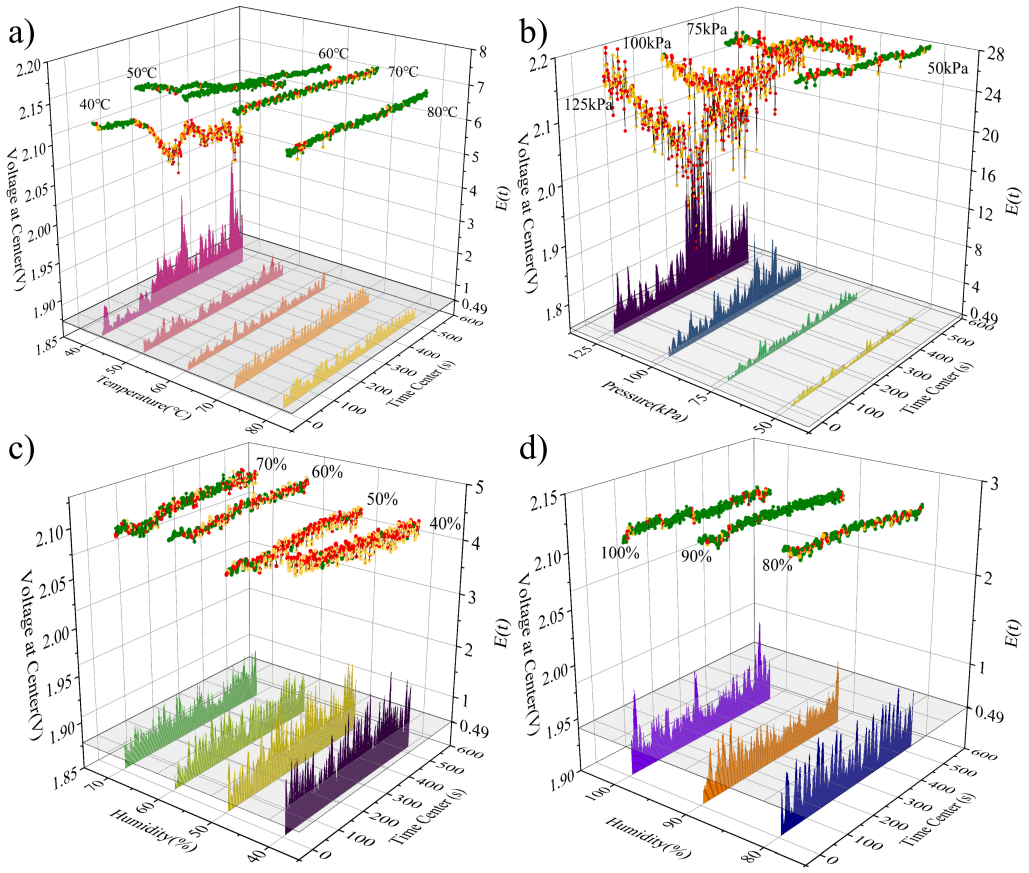

Figure 5: PEMFC voltage dynamics and Lyapunov-like stability responses under varying operating conditions: (a) temperature, (b) backpressure, (c) low-to-moderate humidity, and (d) high humidity.

may offer optimal nominal performance, it appears to introduce water management challenges that potentially destabilize the system. At 80 °C, a slight voltage decline and increased variability in $E(t)$ are observed, consistent with the onset of membrane dehydration or local gas transport limitations [25]. In contrast, under low-temperature conditions (40 °C), the voltage initially appears stable but quickly transitions into a downward trend with amplified fluctuations. The corresponding $E(t)$ values rise steadily and remain above the threshold for extended durations, marking the emergence of persistent instability and eventual voltage collapse.

In Figure 5b, the impact of backpressure on voltage stability is analyzed.

At 50 kPa, the fuel cell operates at a relatively high voltage with minimal dynamic disturbance, and most $E(t)$ values remain well below the stability threshold θ_E, indicating a stable regime. As backpressure increases to 75 kPa, voltage disturbances begin to emerge, accompanied by intermittent threshold crossings in $E(t)$. At 100 kPa and 125 kPa, the system exhibits pronounced instability: voltage traces display marked oscillations and noticeable drops, while $E(t)$ reaches its highest levels across all test conditions. These results suggest that although increased backpressure enhances reactant availability, it may also impede water removal [26], resulting in cathode flooding and eventual localized oxygen starvation and triggering significant instability [27]. The proposed indicator (LSI) effectively captures this transition from kinetically favorable yet dynamically unstable states.

Figures 5c-d explore the influence of humidification on voltage stability. Under low-humidity conditions (40% RH), the voltage exhibits greater fluctuation, although no sharp long-term decline is observed. The primary source of instability arises from increased oscillatory behavior, as reflected by frequent exceedances of the threshold in the $E(t)$ signal. As humidity increases to 60% and 70% RH, the magnitude of voltage fluctuations decreases, and the system gradually transitions toward a more stable state, reflected by reduced variability in $E(t)$. In Figure 5d, further humidification to 90% and 100% RH leads to even more regular voltage trajectories, with most $E(t)$ values remaining below the threshold, indicative of robust operational stability. These results underscore the importance of adequate humidification for maintaining balanced water management and sustaining electrochemical stability in PEMFC systems.

To build upon the findings of the previous section, a statistical overview of voltage stability classification under systematically varied operating conditions is presented in this part. Figure 6 illustrates the distribution of voltage stability states (stable, metastable, and unstable), along with the corresponding statistical behavior of the LSI value $E(t)$ under varying temperature, backpressure, and relative humidity settings. For each parameter group, the left column presents the proportion of each state category, while the right column provides box-and-whisker plots of the computed $E(t)$ across all time windows. The stability threshold ($\theta_E = 0.49$), is indicated by red dashed lines for reference.

With respect to temperature (Figure 6a), the results indicate that at 40 °C, the fuel cell exhibits poor voltage stability: stable windows account for less than 30% of the total, with a large number of time segments classified as

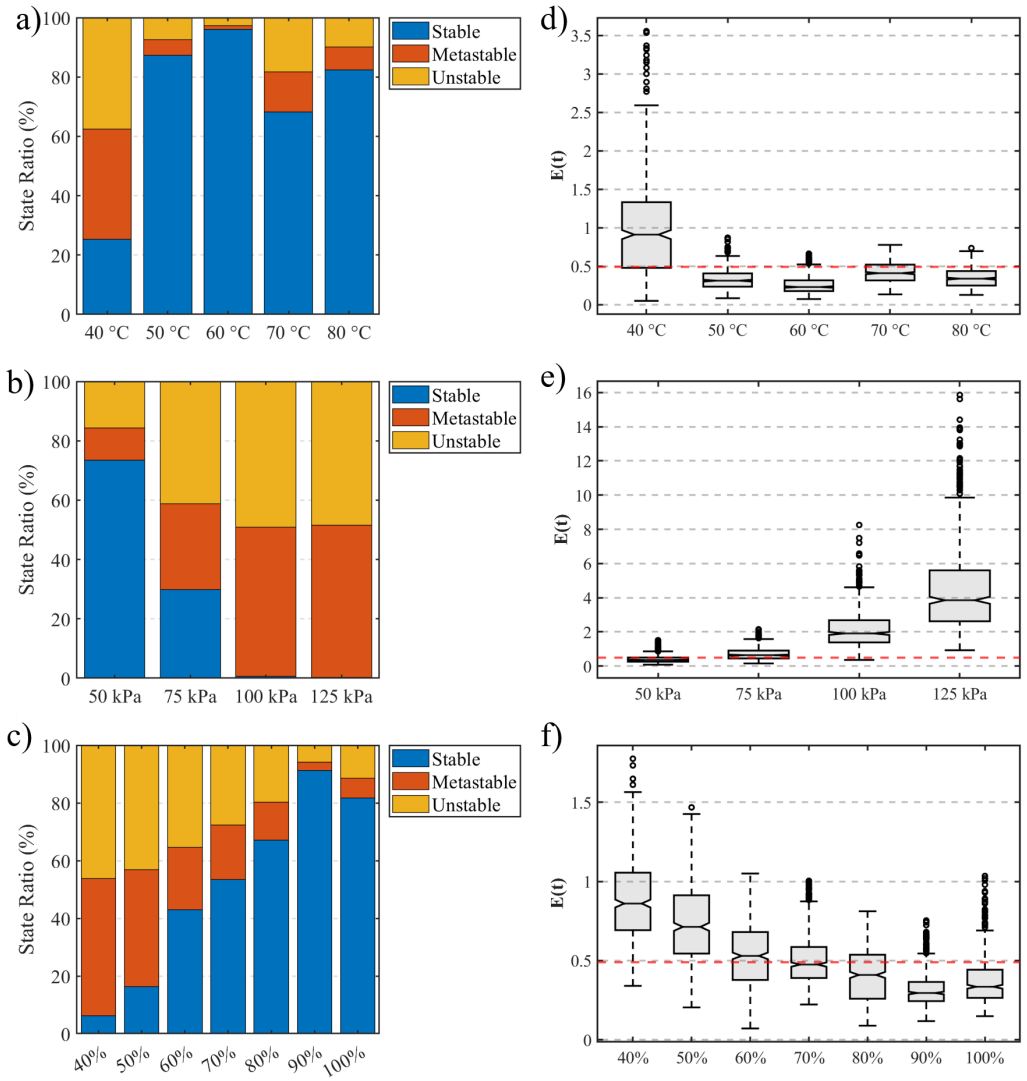

Figure 6: Voltage stability state distributions and corresponding $E(t)$ statistics under different operating conditions: (a) temperature, (b) backpressure, and (c) humidity.

metastable or unstable. The corresponding $E(t)$ distribution is significantly right-skewed, with a median above the stability threshold and multiple high outliers exceeding 3.5, suggesting strong drift and fluctuation. As the temperature increases to 50 °C and 60 °C, voltage stability improves significantly. Stable windows dominate (exceeding 80%), and the entire $E(t)$ distribution falls comfortably below the threshold, with a sharp reduction in both median

and upper whiskers. This improvement is attributed to enhanced reaction kinetics and improved water removal capacity at moderate temperatures. Further increasing the temperature to 70-80 °C results in a slight decline in the proportion of stable windows. However, the median $E(t)$ remains low and well below the instability boundary, indicating that the system continues to operate within a stable regime. These findings are consistent with previous studies, which identify 55-65 °C as the optimal operating range for PEMFCs, providing a balance between electrochemical performance and membrane hydration.

Under different backpressure conditions (Figure 6b), the observed stability trends are markedly nonlinear. At 50 kPa, more than 70% of the data windows are classified as stable, and the corresponding $E(t)$ values are tightly clustered below the threshold, indicating a well-balanced operating condition. Increasing the backpressure to 75 kPa leads to a notable decline in stability, with a sharp reduction in stable windows and a moderate rise in both the interquartile range and upper whiskers of $E(t)$, although the median remains near the threshold. This pattern suggests the emergence of mild transport limitations or localized flooding, which induce frequent but not yet severe disturbances. However, at higher backpressures of 100 kPa and 125 kPa, voltage stability deteriorates significantly: stable windows nearly disappear, and the $E(t)$ distributions exhibit both elevated medians and long upper tails, with extreme values exceeding 15. These results reflect a substantial increase in fluctuation amplitude and persistent voltage degradation, indicative of serious fault conditions. Mechanistically, excessive backpressure is known to hinder liquid water removal from the cathode and increase oxygen transport resistance [28], which aligns with the observed increase in both instability frequency and energetic deviation as captured by $E(t)$.

Under varying humidity conditions (Figure 6c), the system demonstrates a clear sensitivity to membrane hydration [29]. At 40% and 50% RH, stable operation is rare, accounting for less than 20%, and the corresponding $E(t)$ distribution shows elevated medians and wide spreads, highlighting the impact of membrane dehydration and associated increases in ohmic losses. As the RH increases to 60-90%, the fraction of stable windows rises significantly (up to 70-80%), and the $E(t)$ distributions become fully compressed below the threshold, indicating consistently stable performance. This range represents an optimal humidification condition, in which both proton conductivity and water management are effectively balanced. Interestingly, at 100% RH, a minor reduction in stability is observed, along with a slight increase in the

upper whiskers of $E(t)$. This suggests that while membrane hydration is sufficient, localized flooding or excess water retention may begin to compromise system dynamics. These results are consistent with the findings from Kang et al. [30] and Fu et al. [31], who reported that both insufficient and excessive humidification lead to instability, while intermediate RH levels support more stable PEMFC operation.

Taken together, these results establish a comprehensive statistical framework for interpreting PEMFC voltage dynamics across a broad range of operating conditions. By integrating state classification with LSI, this analysis not only quantifies the frequency of stable, metastable and unstable behavior, but also characterizes the severity of deviation through the distribution of $E(t)$. This framework extends the time-domain insights from earlier sections into a generalized, condition-wise perspective, offering practical relevance to fuel cell health monitoring, diagnostic mapping, and control-oriented stability design.

3.3. Stage-wise evolution and mechanism

To validate the physical mechanisms underlying the statistical voltage stability trends observed in Section 3.2, EIS measurements are conducted under each operating condition, as shown in Figure 7. In the Nyquist plots, the scatter points represent the experimentally measured impedance data, while the dashed lines correspond to the fitted spectra obtained using an equivalent circuit model. The fitted curves are used to highlight the overall impedance characteristics and mitigate the influence of measurement noise. The Nyquist plots are grouped by temperature, pressure, and relative humidity. Each impedance spectrum reveals condition-dependent shifts in the high-frequency intercept (associated with membrane resistance), mid-frequency arc size (reflecting charge transfer resistance), and low-frequency tail (indicating mass transport limitations). These electrochemical features provide a mechanistic interpretation of the voltage stability behavior captured by LSI. In particular, increases in charge transfer resistance or mass transport resistance are typically associated with deteriorating electrochemical processes, which manifest as increased voltage fluctuations and drift in the time-domain signals. This behavior is reflected in the evolution of the LSI value $E(t)$, thereby linking the statistical stability indicator with the underlying electrochemical processes of the PEMFC system.

Figure 7a presents the impedance spectra obtained under different temperature conditions. At elevated temperatures of 70-80 °C, the Nyquist plots

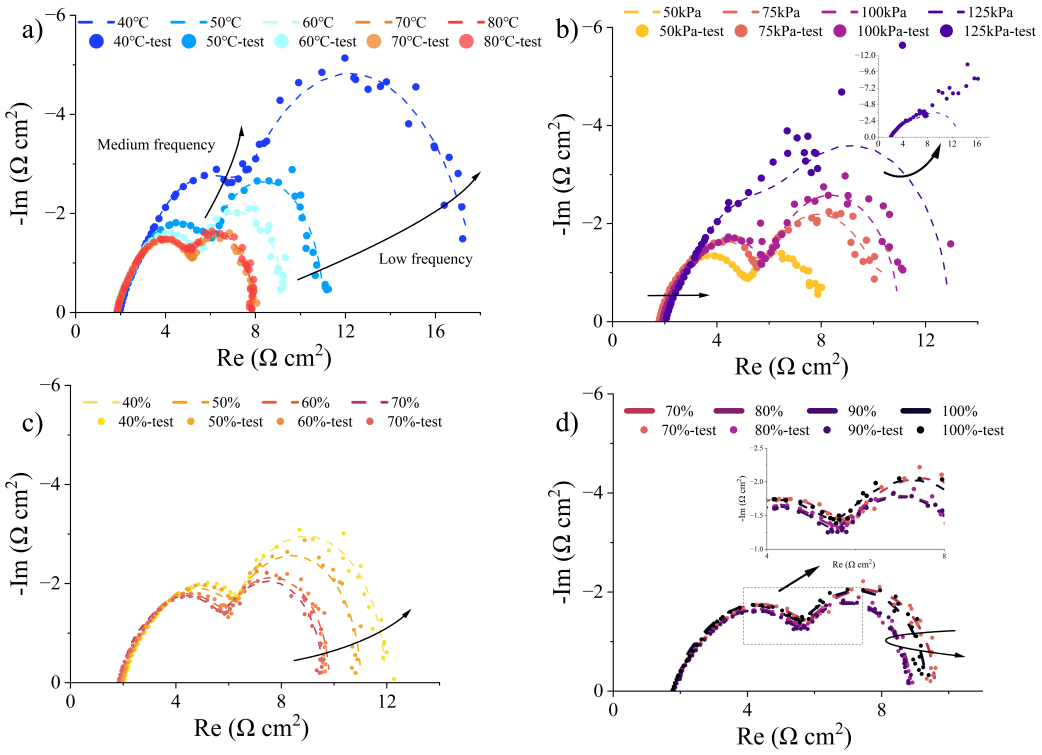

Figure 7: Electrochemical impedance spectra of PEMFC under varying operating conditions: (a) temperature, (b) backpressure, (c) low relative humidity and (d) high relative humidity.

exhibit compressed semicircles, and the high-frequency intercept on the real axis, corresponding to the membrane ohmic resistance R_{ohm}, shifts downward, reflecting enhanced proton conductivity and improved electrochemical kinetics. These features are consistent with the low $E(t)$ values and stable voltage behavior previously observed in Figures 5a and 6a. At intermediate temperatures of 50-60 °C, a moderate expansion of the mid-frequency arc is observed, while the low-frequency region becomes more pronounced, indicating a rise in charge transfer resistance and the onset of mass transport limitations. At 40 °C, the arcs enlarge substantially and deviate from the ideal semicircular shape, extending into the low-frequency region with a pronounced tail. This behavior suggests sluggish electrochemical kinetics and limited oxygen transport at the cathode. Moreover, the visible divergence between the experimental and fitted curves in the low-frequency range points to nonlinear dynamic responses, aligning with the elevated $E(t)$ values and

a higher proportion of unstable windows under low-temperature operation.

Figure 7b highlights the impact of increasing backpressure on the impedance response. As the pressure rises from 50 to 125 kPa, the low-frequency tail of the Nyquist plot extends significantly and steepens, indicating a marked rise in Warburg-type diffusion impedance. This behavior suggests impaired oxygen transport through the gas diffusion and catalyst layers, likely caused by liquid water accumulation in the cathode. At 125 kPa, the impedance trace diverges sharply at low frequency, approaching a 45° slope, a hallmark of diffusion-limited transport. The deviation between experimental and fitted data becomes particularly pronounced at low frequencies, reflecting a transition to a polarization-limited regime. These findings are in line with the sharp rise in $E(t)$ and the dominance of unstable voltage states observed in Figure 5b and Figure 6b, supporting the conclusion that cathode flooding and gas starvation are key mechanisms driving instability under high-pressure conditions [21].

Figure 7c-d show the impedance behavior under varying RH conditions. At low RH levels (40-50%), the impedance arcs broaden across the frequency spectrum, particularly in the low frequency region, indicating an increase in ohmic resistance (R_{ohm}) and a reduction in ionic conductivity due to insufficient membrane hydration. The presence of large diffusion impedance suggests non-uniform current distribution, likely caused by uneven membrane hydration and spatial variation in active reaction zones. Similar humidity-dependent impedance trends have also been reported by Fu et al. [31]. These unfavorable electrochemical conditions correspond to voltage oscillations, as reflected by the increased and fluctuating $E(t)$ values. As RH increases to 60-70%, both ohmic and charge transfer resistances decrease, and the impedance arcs become more compact, indicating improved proton conductivity and more uniform electrochemical activity. Optimal performance is observed between 80% and 90% RH, where the impedance profiles are most compact and the corresponding $E(t)$ values reach their lowest levels, suggesting highly stable operation. At 100% RH, a slight re-appearance of curvature in the low-frequency region and a shallow diffusion tail suggest the onset of electrode flooding, likely due to vapor condensation. This interpretation is further supported by a slight increase in $E(t)$ variance observed in Figure 6c, pointing to incipient instability under over-saturated humidification.

In summary, the impedance characteristics shown in Figure 7 provide electrochemical validation for the voltage stability states classified by LSI time-varying value $E(t)$. Elevated $E(t)$ values correspond to increased re-

sistive or diffusion losses, as observed under low temperature, insufficient humidification, or excessive backpressure conditions. In contrast, low $E(t)$ values are associated with minimized impedance arcs and suppressed mass transport limitations, reflecting balanced system operation and robust electrochemical performance. These results affirm the effectiveness of LSI not only as a dynamic voltage stability indicator, but also as a real-time proxy for capturing the evolution of internal impedance characteristics in PEMFCs. At the present stage, this linkage should be understood as a condition-wise mechanistic interpretation rather than a direct parametric mapping between $E(t)$ and individual impedance elements; establishing such a quantitative mapping will require synchronized state-resolved EIS measurements in future work.

To further investigate the underlying mechanisms of fuel cell instability under representative fault conditions, this study examines the temporal evolution of cell voltage and the corresponding LSI through a three-stage transition pathway. Figure 8-10 visualizes the dynamic trajectory of the system in a three-dimensional state space, defined by voltage, $E(t)$, and time, where each point along the trajectory is color-coded according to its classified stability state, enabling intuitive visualization of transitions between stable, metastable, and unstable regimes.

To elucidate the instability mechanisms under typical low-temperature fault scenarios, a time-resolved analysis of the voltage response and the corresponding LSI value $E(t)$ is conducted. Figure 8 depicts the three-dimensional evolution of voltage, $E(t)$, and time under the 40 °C condition, with each point labeled according to its classified stability states. In the early phase (0-200 s), the system remains predominantly stable, as evidenced by low $E(t)$ values and relatively smooth voltage progression. This suggests a kinetically moderate but electrochemically stable operating state, where mass transport effects have not yet become limiting. As the cell continues to operate, a gradual voltage decline, accompanied by rising $E(t)$ indicates the emergence of instability. This intermediate phase (200-250 s) is characterized by a directional, non-oscillatory degradation trend, typical of drift-dominated metastable behavior. The underlying mechanism is likely associated with liquid water accumulation resulting from limited evaporation at low temperatures, which gradually impairs oxygen diffusion pathways in the cathode [32]. Beyond 250 s, the system enters a highly unstable regime, marked by strong temporal oscillations in both voltage and $E(t)$. This third stage exhibits a spiraling descent in the state space, indicative of nonlinear feed-

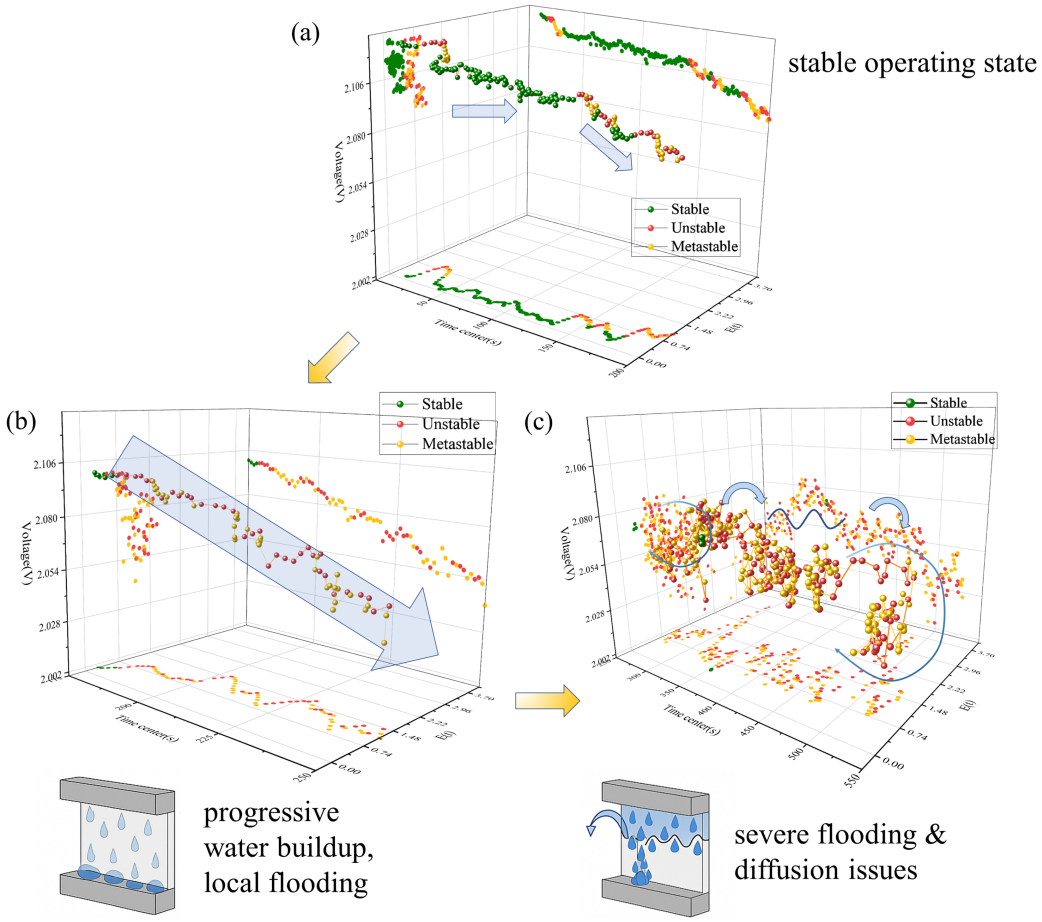

Figure 8: Voltage dynamics and stability evolution under low-temperature conditions: (a) Phase 1, (b) Phase 2, (c) Phase 3.

back instability. Such behavior is consistent with the onset of severe mass transport limitations, where oxygen starvation and transient localized flooding introduce self-reinforcing dynamic disturbances. At this stage, the low temperature further aggravates the situation by suppressing gas diffusivity and prolonging liquid water residence time, thereby preventing the recovery of stable operating conditions [33]. The combined effects manifest as large, sustained oscillations superimposed on a declining voltage baseline, aligning with the high variability in $E(t)$. Overall, this staged transition, from stability to metastability, and ultimately to chaotic instability, highlights a fault evolution pathway fundamentally driven by thermally constrained water

management and its impact on reactant gas transport [34]. This interpretation is further supported by the impedance data shown in Figure 7a, where a significant enlargement of the low-frequency arc is observed under the 40 °C condition. The pronounced increase in diffusion-related impedance confirms the presence of mass transport limitations, consistent with the observed voltage degradation and elevated $E(t)$ values during the later stages of the fault evolution.

Under high backpressure (125 kPa), the voltage stability of the fuel cell shows a significant stage-wise dynamic evolution. The three-dimensional time-series diagram in Figure 9 reveals its characteristic behavior and potential underlying mechanism across three distinct phases. In phase 1 (0-250

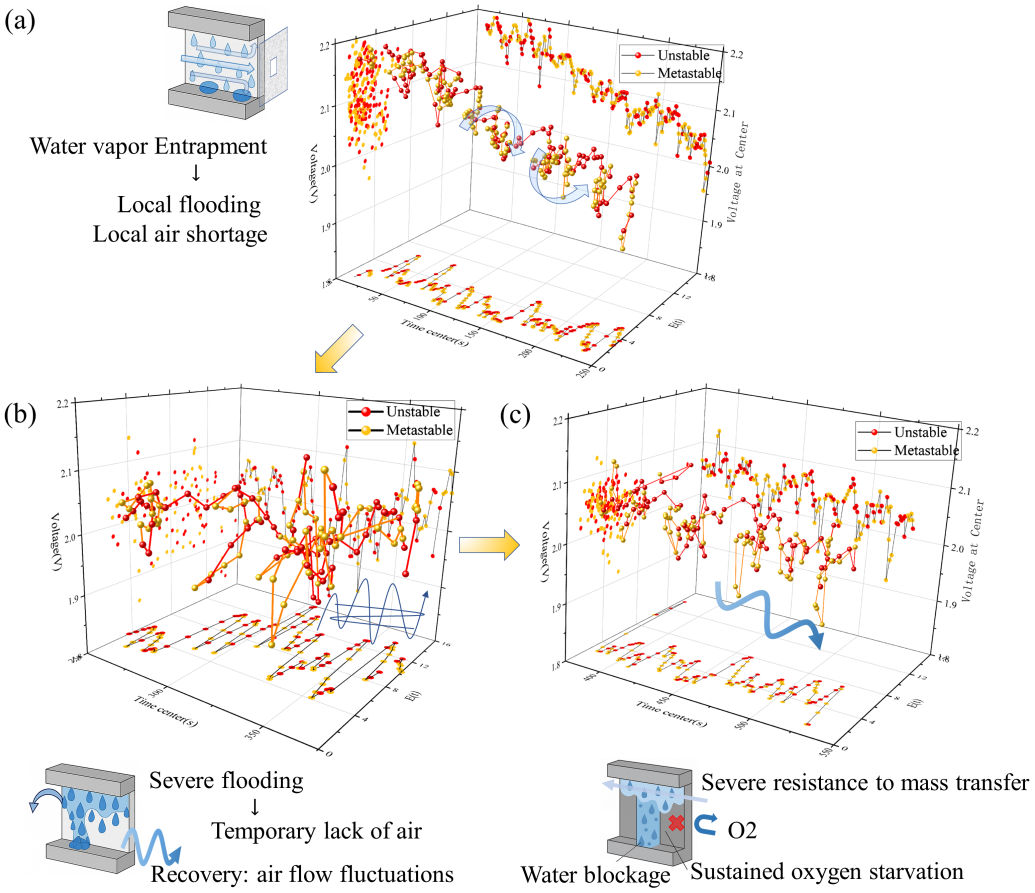

Figure 9: Voltage dynamics and stability evolution under high backpressure: (a) Phase 1, (b) Phase 2, (c) Phase 3.

s), the system enters an early instability accumulation phase. During this period, the voltage displays a fluctuating downward trend, accompanied by obvious localized high-frequency oscillations, while the overall $E(t)$ values remain at medium levels. This phenomenon is usually related to localized mass transport limitations on the gas diffusion side. Although elevated backpressure initially improves oxygen transport capacity, it also increases the retention and aggregation of water in the electrode pores, resulting in oxygen penetration obstruction in some areas. In addition, excessive pressure may promote liquid water redistribution in the porous structure, resulting in spatial inhomogeneity in local reaction environments. These variations give rise to electrochemical non-uniformity and microscale voltage fluctuations, consistent with prior findings on pressure-induced heterogeneity [35].

As the system transitions into Phase 2 (250-400 s), the instability becomes more pronounced. This stage is marked by a rapid rise in $E(t)$ and pronounced voltage oscillations with a sawtooth-like profile. Such nonlinear fluctuations suggest the system has entered a critical transitional regime, likely dominated by intermittent polarization dynamics. A plausible underlying mechanism is the emergence of a "flooding-recovery" cycle at the catalyst layer [36], wherein localized oxygen starvation occurs due to transient water accumulation, followed by brief reactivation driven by pulsed exhaust control via the backpressure valve [37]. These spatially dynamic water redistributions modulate the gas-liquid interface, intermittently disturbing the triple-phase boundary, and thereby triggering abrupt voltage disturbances. Moreover, the ventilation capacity at this high backpressure level appears insufficient to effectively expel accumulated liquid water, thus amplifying the temporal volatility of the electrochemical environment and reinforcing the instability of the system.

In Phase 3 (>400 s), although $E(t)$ remains consistently elevated, the intensity of voltage fluctuations visibly declines compared to the preceding phase. The system appears to enter the late stage of the fault evolution, characterized by a progressively declining voltage baseline, as evidenced by the increasingly lower troughs in the three-dimensional trajectory. This behavior may reflect a transition into a low-activity regime, in which portions of the electrode become chronically oxygen-starved due to extensive water blockage [38], effectively damping further dynamic responsiveness. The presence of multiple foldback patterns in the voltage-time trajectory may represent a "breathing" response of the local electrode: intermittent recovery of electrochemical activity followed by rapid re-destabilization. Such cyclic

behavior suggests that the system is approaching a critical failure state. The impedance spectrum shown in Figure 7b supports this interpretation: the prominent extension of the low-frequency arc and the steepening of the tail response under 125 kPa indicate severe mass transport resistance, consistent with the overall elevated $E(t)$ level and the accumulation of polarization effects, reinforcing the notion that gas-liquid transport limitations play a central role in governing the dynamic stability of the cell.

Under low-humidity (dry) operating conditions (Figure 10), the voltage dynamics of the PEMFC follow a distinct evolutionary pathway, fundamentally different from the liquid-water-driven fault modes. The three-dimensional time-series trajectory reveals an overall pattern of moderate-amplitude, quasi-periodic oscillations. This behavior suggests that although the system displays a measurable instability, it does not progress along a flooding-dominated polarization path. Instead, the observed fluctuations are more likely governed by membrane dehydration and localized reactant undersupply, reflecting a water transport-limited mechanism. The presence of regular sawtooth-like voltage perturbations, which are highlighted by the blue arrow in Figure 10, points to a dominant frequency-governed disturbance mode, often associated with transient oxygen starvation in the cathode gas channel. Under dry conditions, insufficient product water fails to maintain adequate membrane hydration, and the incoming airflow is unable to effectively redistribute moisture across the active area. Consequently, local proton conductivity is degraded [39], producing spatiotemporal instabilities. Notably, unlike the abrupt voltage collapses observed under high-humidity flooding, the system undergoes a repetitive cycle of mild passivation, minor

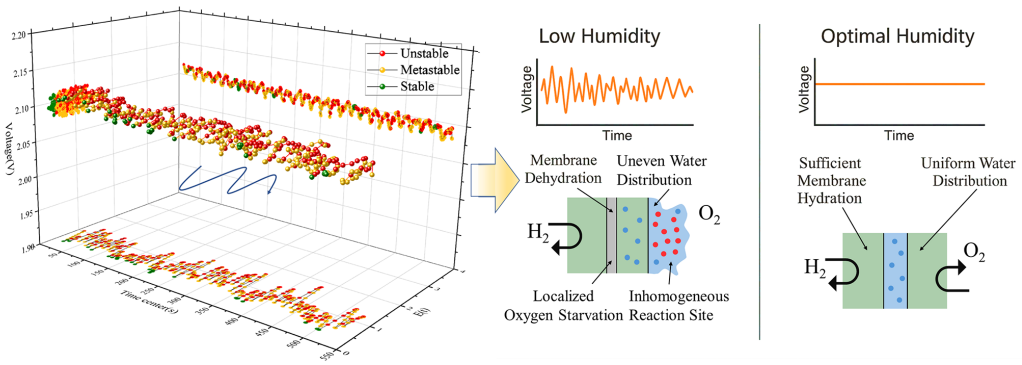

Figure 10: Voltage dynamics and stability evolution under low humidity conditions.

voltage dips, and partial recovery, consistent with a mechanism dominated by proton transport degradation and gas-phase heterogeneity. In summary, the voltage dynamics of PEMFCs under typical fault conditions, including low temperature, high backpressure, and low humidity, exhibit distinct evolutionary trajectories, each governed by specific transport and reaction limitations. Low-temperature operation triggers a gradual decline into instability, primarily driven by impaired oxygen diffusivity and prolonged water retention, ultimately resulting in severe mass transport resistance and chaotic fluctuations. High backpressure accelerates instability through liquid water accumulation and redistribution within porous media, leading to a multi-stage evolution marked by flooding-recovery cycles and eventual oxygen starvation. In contrast, low-humidity conditions do not cause catastrophic polarization but result in persistent, low-amplitude oscillations driven by membrane dehydration and uneven gas-phase distribution. Across all scenarios, the LSI effectively captures the onset, intensity, and temporal evolution of voltage instability. Its strong correlation with electrochemical impedance characteristics enables a unified and physically interpretable framework for assessing fuel cell degradation. These findings underscore the potential of LSI as a real-time dynamic diagnostic metric for identifying both abrupt and marginal failure mechanisms in PEMFC systems.

4. Conclusion

This study proposes a data-driven signal analysis framework for dynamic voltage stability assessment in proton exchange membrane fuel cells. A Lyapunov-inspired stability indicator, the Lyapunov-like Stability Indicator (LSI), is developed by combining voltage drift rate and volatility within a sliding time window. The resulting time-dependent indicator $E(t)$ enables real-time identification of system dynamics and classification of operating states into stable, metastable, and unstable regimes through a statistical threshold determined using Kernel Density Estimation.

Based on this indicator, a stability landscape was established under 16 experimentally controlled operating conditions, revealing clear relationships between temperature, humidity, backpressure, and voltage stability behavior. The results show that optimal humidification (70–90% RH) maintains predominantly stable operation, while excessive backpressure leads to persistent instability. Temperature exhibits a strong regulatory role, with the most favorable stability observed around 60–70 °C.

To further interpret the mechanisms underlying voltage instability, impedance spectroscopy was integrated with time-domain voltage analysis to reconstruct representative fault evolution pathways. The results indicate that low temperature, high backpressure, and low humidity lead to distinct instability behaviors associated with mass transport limitation, flooding–recovery cycles, and membrane dehydration, respectively. The proposed indicator successfully tracks the onset and evolution of these instability processes and provides an interpretable measurement-based tool for PEMFC stability monitoring.

Overall, the proposed framework links time-domain voltage dynamics with electrochemical impedance characteristics, offering a practical methodology for stability assessment and early fault detection in PEMFC systems. The present results should be interpreted as a measurement-oriented proof of concept based on a single partially degraded three-cell stack under controlled laboratory conditions; accordingly, the reported thresholds and regime distributions should not yet be regarded as universally transferable limits. Future work will explore more quantitative relationships between stability regime transitions and impedance characteristics through synchronized EIS measurements, repeated experiments, and validation across different stack configurations, MEA materials, and operating profiles.

Declarations

- **Funding:**
  Funding information has been removed for double-blind review.

- **Conflicts of interest:**
  The authors have no conflicts of interest to declare that are relevant to the content of this article.

- **Data availability:**
  Data will be made available on request.

References

[1] M. A. Aminudin, et al., An overview: Current progress on hydrogen fuel cell vehicles, International Journal of Hydrogen Energy 48 (2023) 4371–4388. doi:10.1016/j.ijhydene.2022.10.156.

[2] N. A. A. Qasem, G. A. Q. Abdulrahman, A recent comprehensive review of fuel cells: History, types, and applications, International Journal of Energy Research 2024 (2024). doi:10.1155/2024/7271748.

[3] H. Yuan, H. Dai, P. Ming, X. Wang, X. Wei, Quantitative analysis of internal polarization dynamics for polymer electrolyte membrane fuel cell by distribution of relaxation times of impedance, Applied Energy 303 (2021). doi:10.1016/j.apenergy.2021.117640.

[4] Z. K. Luo, et al., Dynamic response characteristics and water-gas-heat synergistic transport mechanism of proton exchange membrane fuel cell during transient loading, Energy 302 (2024). doi:10.1016/j.energy.2024.131852.

[5] O. S. Ijaodola, et al., Energy efficiency improvements by investigating the water flooding management on proton exchange membrane fuel cell (pemfc), Energy 179 (2019) 246–267. doi:10.1016/j.energy.2019.04.074.

[6] A. Khanafari, A. Alasty, M. J. Kermani, S. Asghari, Flooding and dehydration diagnosis in a polymer electrolyte membrane fuel cell stack using an experimental adaptive neuro-fuzzy inference system, International Journal of Hydrogen Energy 47 (2022) 34628–34639. doi:10.1016/j.ijhydene.2022.08.063.

[7] F. Xiao, T. Chen, Z. Y. Gan, R. X. Zhang, The influence of external operating conditions on membrane drying faults of proton-exchange membrane fuel cells, Energy 285 (2023). doi:10.1016/j.energy.2023.128787.

[8] Z. R. Guo, H. Chen, H. Guo, F. Ye, Low humidification effect on performance of proton exchange membrane fuel cells under high current density conditions, International Communications in Heat and Mass Transfer 155 (2024). doi:10.1016/j.icheatmasstransfer.2024.107505.

[9] Z. Y. Kang, S. M. Alia, M. Carmo, G. Bender, In-situ and in-operando analysis of voltage losses using sense wires for proton exchange membrane water electrolyzers, Journal of Power Sources 481 (2021). doi:10.1016/j.jpowsour.2020.229012.

[10] G. H. Yang, Q. H. Deng, Y. Zhou, W. S. Chen, B. Chen, Dynamic evolutions of local current density and water-gas distribution of proton exchange membrane fuel cell with dead-ended anode, Energy Conversion and Management 298 (2023). doi:10.1016/j.enconman.2023.117777.

[11] W. Tang, et al., A new insight into the in-plane heterogeneity of commercial-sized fuel cells via a novel distribution-based method, Applied Energy 368 (2024). doi:10.1016/j.apenergy.2024.123484.

[12] S. D. Li, et al., Qualitative and quantitative diagnosis of internal hydrogen leakage in fuel cell based on air flowrate control and open-circuit voltage measurements, Electrochimica Acta 477 (2024). doi:10.1016/j.electacta.2024.143821.

[13] L. Zhao, et al., A novel pre-diagnosis method for health status of proton exchange membrane fuel cell stack based on entropy algorithms, ETransportation 18 (2023). doi:10.1016/j.etran.2023.100278.

[14] D. Benouioua, D. Candusso, F. Harel, P. Picard, Diagnosis of fuel cells using instantaneous frequencies and envelopes extracted from stack voltage signal, International Journal of Hydrogen Energy 47 (2022) 9706–9718. doi:10.1016/j.ijhydene.2022.01.046.

[15] J. Li, et al., Spatial–temporal synchronous fault feature extraction and diagnosis for proton exchange membrane fuel cell systems, Energy Conversion and Management 315 (2024). doi:10.1016/j.enconman.2024.118771.

[16] Z. Liu, et al., A novel method for polymer electrolyte membrane fuel cell fault diagnosis using 2d data, Journal of Power Sources 482 (2021) 228894. doi:10.1016/j.jpowsour.2020.228894.

[17] Z. K. Luo, et al., Evolution of current distribution and performance degradation mechanism of pemfc during transient loading under gas starvation condition: An experimental study, Applied Energy 388 (2025). doi:10.1016/j.apenergy.2025.125702.

[18] X. N. Zhu, et al., Effects of operating conditions on the performance uniformity of the proton-exchange membrane fuel cell stack, Energy Conversion and Management 281 (2023). doi:10.1016/j.enconman.2023.116856.

[19] P. Ren, et al., Diagnosis of water failures in proton exchange membrane fuel cell with zero-phase ohmic resistance and fixed-low-frequency impedance, Applied Energy 239 (2019) 785–792. doi:10.1016/j.apenergy.2019.01.235.

[20] Y. B. Shao, et al., New insights into steady-state multiplicity in polymer electrolyte membrane fuel cell, Journal of Power Sources 554 (2023). doi:10.1016/j.jpowsour.2022.232328.

[21] B. B. Hu, Z. G. Qu, W. Q. Tao, A comprehensive system-level model for performance evaluation of proton exchange membrane fuel cell system with dead-ended anode mode, Applied Energy 347 (2023). doi:10.1016/j.apenergy.2023.121327.

[22] X. Sun, et al., Hybrid ensemble learning model for predicting external characteristics of proton exchange membrane fuel cells under various operating conditions, Energy 323 (2025) 135913. doi:10.1016/j.energy.2025.135913.

[23] X. Sun, et al., Boosted deep neural network model for forecasting the electrochemical impedance of a proton exchange membrane fuel cell under varying operating conditions, Renewable Energy 256 (2026) 124099. doi:10.1016/j.renene.2025.124099.

[24] J. Fu, et al., Synergistic optimization for inlet parameters of proton exchange membrane fuel cells based on improved fuzzy grey relational analysis, Thermal Science and Engineering Progress 55 (2024) 103008. doi:10.1016/j.tsep.2024.103008.

[25] G. Li, W. Kujawski, E. Rynkowska, Advancements in proton exchange membranes for high-performance high-temperature proton exchange membrane fuel cells (ht-pemfc), Reviews in Chemical Engineering 38 (2022) 327–346. doi:10.1515/revce-2019-0079.

[26] G. Zhang, X. Xie, B. Xie, Q. Du, K. Jiao, Large-scale multi-phase simulation of proton exchange membrane fuel cell, International Journal of Heat and Mass Transfer 130 (2019) 555–563. doi:10.1016/j.ijheatmasstransfer.2018.10.122.

[27] J. P. Owejan, et al., Voltage instability in a simulated fuel cell stack correlated to cathode water accumulation, Journal of Power Sources 171 (2007) 626–633. doi:10.1016/j.jpowsour.2007.06.174.

[28] S. Hong, G. Liejin, L. Hongtan, The effect of operating parameters on water transport in pem fuel cells, Heat Transfer – Asian Research 35 (2006) 89–100. doi:10.1002/htj.20107.

[29] S. Shimpalee, S. Greenway, D. Spuckler, J. W. Van Zee, Predicting water and current distributions in a commercial-size pemfc, Journal of Power Sources 135 (2004) 79–87. doi:10.1016/j.jpowsour.2004.03.059.

[30] J. W. Kang, et al., Experimental study of voltage uniformity and stability of h_2/o_2 pem fuel cell stack with dead-end anode and recirculation cathode, Sustainable Energy Technologies and Assessments 72 (2024). doi:10.1016/j.seta.2024.104052.

[31] J. Fu, et al., Experimental investigation for the influence mechanism of air intake method and humidity level on performance of proton exchange membrane fuel cells, International Journal of Hydrogen Energy 86 (2024) 823–834. doi:10.1016/j.ijhydene.2024.08.497.

[32] R. M. Mensharapov, N. A. Ivanova, D. D. Spasov, A. V. Bakirov, V. N. Fateev, Pemfc performance at nonstandard operating conditions: A review, International Journal of Hydrogen Energy 96 (2024) 664–679. doi:10.1016/j.ijhydene.2024.11.395.

[33] R. Banerjee, S. G. Kandlikar, Liquid water quantification in the cathode side gas channels of a proton exchange membrane fuel cell through two-phase flow visualization, Journal of Power Sources 247 (2014) 9–19. doi:10.1016/j.jpowsour.2013.08.016.

[34] X. R. Wang, et al., Review on water management methods for proton exchange membrane fuel cells, International Journal of Hydrogen Energy 46 (2021) 12206–12229. doi:10.1016/j.ijhydene.2020.06.211.

[35] F. B. Baz, R. M. Elzohary, S. Osman, S. A. Marzouk, M. Ahmed, A review of water management methods in proton exchange membrane fuel cells, Energy Conversion and Management 302 (2024). doi:10.1016/j.enconman.2024.118150.

[36] Y. H. Li, et al., Novel approach to determine cathode two-phase-flow pressure drop of proton exchange membrane fuel cell and its application on water management, Applied Energy 190 (2017) 713–724. doi:10.1016/j.apenergy.2017.01.010.

[37] J. Zhao, et al., Visualization study on the effect of pulsating flow on the two-phase dynamic behavior of proton exchange membrane fuel cells in

dead-ended anode mode, Energy 330 (2025). doi:10.1016/j.energy.2025.136919.

[38] P. Ren, et al., Diagnosis and mechanism analysis of startup-shutdown-induced fuel cell degradation in stack-level, Energy Conversion and Management 269 (2022). doi:10.1016/j.enconman.2022.116140.

[39] N. Wang, Z. Qu, G. Zhang, Modeling analysis of polymer electrolyte membrane fuel cell with regard to oxygen and charge transport under operating conditions and hydrophobic porous electrode designs, eTransportation 14 (2022) 100191. doi:10.1016/j.etran.2022.100191.